ACS APPLIED MATERIALS & INTERFACES

Research Article

www.acsami.org

Photoluminescent SBA-16 Rhombic Dodecahedral Particles: Assembly, Characterization, and ab Initio Modeling

Juan M. Ruso,[†] Victor Pardo,[†,‡] Javier Sartuqui,[§] Noel Gravina,[§] Noelia L. D'Elía,[§] Olga I. Pieroni,[§] and Paula V. Messina*[,§]

[†]Department of Applied Physics, University of Santiago de Compostela, Santiago de Compostela 15701,Spain

[‡]Technological Research Institute, University of Santiago de Compostela, Santiago de Compostela 15701, Spain

[§]Department of Chemistry, INQUISUR-CONICET, Universidad Nacional del Sur, Av. Alem 1253, Bahía Blanca 8000, Argentina

Supporting Information

ABSTRACT: Nowadays, the use of polyhedral instead of spherical particles as building blocks of engineering new materials has become an area of particular effort in the scientific community. Therefore, fabricating in a reproducible manner large amounts of uniform crystal-like particles is a huge challenge. In this work we report a low reagent-consuming binary surfactant templated method mediated by a hydrothermal treatment as a facile and controllable route for the synthesis of crystal-like rombdodecahedral particles exhibiting SBA-16 mesoporosity. It was determined that the hydrothermal treatment conditions were a key point upon the final material morphology, surface area, microporosity, wall thickness, and mesopore width. As a consequence of their internal mesoporosity order, rhombic dodecahedral synthesized particles exhibited highly efficient ultraviolet absorptions and photoluminescence emissions at room temperature. Conducting experimental and theoretical comparative studies allowed us to infer that the presence of intrinsic defects confined into an ordered mesoporous structure plays a very important role in semiconductor materials. The information presented here is expected to be useful, giving new, accurate information, for the construction of novel technological devices.

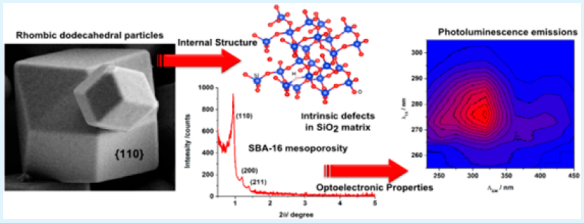

KEYWORDS: *rombdodecahedral particles, SBA-16, photoluminescence emissions, ab initio modeling, hydrothermal treatment*

1. INTRODUCTION

Because of their vast importance in both theoretical and practical applications, a central subject in materials science is the engineering of particles that can be self-assembled into intricate structures.[1,2] The variability in size and composition of the building blocks of these two- or three-dimensional (2-D or 3-D) structures enables them to exhibit many useful properties, which are attractive for certain applications, including microelectronics and optoelectronic devices, biological and chemical sensors, adsorbents, hosts for nanoclusters synthesis, and several more.[2−5] The presence of periodic ordered mesopores is an extra value that can be added to such particles and to the macrostructures built from them.[3] Since the first report on the ionic surfactant templated synthesis of hexagonally ordered mesoporous silica,[6] MCM-41, the ordered mesoporous materials (OMMs) have been studied extensively.[7−9] A significant advance in this area was introduced by the application of nonionic triblock copolymer ($EO_xPO_yEO_x$) to template OMMs.[10,11] This results in the SBA (SBA = Santa Barbara) family such as SBA-15[12] and SBA-16[13,14] that became very popular materials because of their larger mesopores, thicker pore walls, and higher hydrothermal stability in comparison with their counterparts in the M41S family. In particular, SBA-16 exhibits a 3-D cubic arrangement of cylindrical mesopores where each one is linked with its eight nearest neighbors and, in contrast to M41S materials, is interconnected by irregular micropores.[13,15] The micropores in the wall of SBA-16 originated from the hydrophilic ethylene oxide (EO) chains which penetrate the silica wall during synthesis and leave microporosity after calcination.[13] This dual-porosity system makes the SBA materials superior candidates for several of the aforementioned applications.[14] To date, considerable advances have been achieved toward the fabrication of ordered structures of spherical colloidal particles displaying or not displaying mesoporosity.[16−18] However, such morphology is not the best option for the construction of 2-D or 3-D frameworks; for example, self-assembled ordered macrostructures of spherical particles used as photonic crystals cannot achieve complete band gaps due to the degeneracy of the polarization models induced by their symmetry.[4] Non-spherical particles can break the symmetry induced degeneracy providing direct advantages over their spherical counterparts for the construction of ordered structures with high complexity.[19,20] Therefore, the elaboration of effective and non-time-consuming recipes for the fabrication of micrometer polyhedral particles is of great interest, in particular those containing a

Received: February 20, 2015
Accepted: May 27, 2015

DOI: 10.1021/acsami.5b01637
ACS Appl. Mater. Interfaces XXXX, XXX, XXX−XXX

periodic arrangement of mesopores, like ordered SBA-16. Numerous theoretical and experimental studies have been performed in order to design the morphology as well as the mesostructure of mesoporous materials, such as films,[21] spheres,[22] micrometer patterning hollow tubular shapes,[23] fibers,[24] and other anisotropic shapes.[25] However, it is not common for a periodic mesoporous material to show a crystal-like well-defined external morphology. For example, Kim and Ryoo[26] have reported the synthesis of MCM-48 crystals (*Ia*3*d*) with truncated rhombic dodecahedral shape. Guan[27] and Sayari et al.[28] have shown the preparation of hybrid cubic mesoporous crystals (P*m*3*n*) with well-defined decaoctahedron form. Also, Che and co-workers[29] have reported the synthesis of SBA-1 (P*m*3*n*) mesoporous material with crystal morphologies and pore sizes less than 4 nm. Yu et al.[30] have reported the first synthesis of cubic mesoporous (I*m*3*m*) silica single rhombdodecahedron shape crystal of 1 μm diameter and uniform large mesopores up to 7.4 nm using a commercial nonionic block copolymer under acidic conditions and inorganic salts to increase the interaction between silicate species and nonionic surfactants. To the best of our knowledge, a road map for the development of mesophases with particular geometry characteristics, mainly for particles grown from aqueous solutions with dilute surfactant concentration, is still incomplete.

Here we present a simple methodology to prepare silica rhombic dodecahedral particles up to 4 μm diameter reducing the F127/TEOS, F127/CTAB, and HCl/TEOS molar ratio to 0.0005, 0.016, and 1, respectively. Particles exhibit hexagonal SBA-16 mesoporosity and ultraviolet photoluminescent (UV-PL) emissions at room temperature. The materials studied here were obtained via a two-step hydrothermal synthesis under less acidic conditions (0.76 M HCl) than the conventional protocols,[13,30] and involve an initial self-assembly of the cationic−nonionic surfactant mixture and silica species at 40 °C followed by an extensive hydrothermal treatment at 100−120 °C over 24 h. The samples were highly ordered, as evidenced by SAXD, showing reflection peaks characteristic of the *Im*3*m* symmetry group. The hydrothermal treatment conditions revealed a remarkable effect upon the final material crystal-like morphology, surface area, microporosity, wall thickness, mesopore width, and optoelectronic properties. The influence of the hexadecyltrimethylammonium cationic surfactant and the amphiphilic triblock copolymer has also been discussed.

Motivated by technological implications of UV-PL defects in the physical properties of SiO_2-based devices for fiber optics, a great deal of work was done in the past two decades to identify their structure.[31−33] However, experimental measurement of the energy gap of nanostructures is very challenging, and appropriate data are needed to clarify this important point. For these reasons, the optical properties of the materials have been analyzed by experimental and theoretical approaches (DFT). The excellent agreement obtained by both methods allows us to infer the origins of the optical properties of the materials at the atomic scale. The simplicity of the proposed synthesis approach and the material photoluminescent properties should open a new door for the attainment of SBA-16 polyhedral particles, and their potential uses as the building blocks of complex macrostructures with unique applications such as photonic crystals.

2. EXPERIMENTAL SECTION

2.1. Reagents. Hexadecyl-trimethylammonium bromide (CTAB, MW = 364.48 g mol^{-1}, 99%, Sigma), triblock copolymer Pluronic F127 ($EO_{106}PO_{70}EO_{106}$, EO = ethylene oxide, PO = propylene oxide, MW = 12 500 g mol^{-1}, Sigma), hydrochloride acid (HCl, 11.8 mol L^{-1}, ρ = 1.18 g cm^{-3}, Sigma), and sodium tetraethyl orthosilicate (TEOS, MW = 208.33 g mol^{-1}, 98%, Aldrich) were used without further purification. For solution preparation, only triple-distilled water was used.

2.2. Material Synthesis. Rhombic dodecahedron SBA-16 particles were prepared by using F127 and CTAB as binary templates in acidic aqueous solution (0.750 mol L^{-1} HCl) at 40 °C. The synthesis method was obtained by comparing different literature procedures.[8,14,34] Typically, F127 (0.123 g), H_2O (6.65 cm^3), CTAB (17.5 cm^3, 0.035 mol L^{-1}), and concentrated hydrochloric acid (1.65 cm^3, 11.8 mol L^{-1}) were mixed together, heated at 40 °C, and sonicated for 10 min in a Teflon-stoppered test tube to form a clear solution. Then, 4.25 cm^3 of TEOS was added to the previously prepared solution under stirring at 500 rpm. After 10 min of stirring, the mixture was allowed to stand under hydrothermal conditions at 100−120 °C for 24 h in an autoclave. The obtained material was filtered, washed with triple-distilled water, and left to dry at room temperature. Finally, it was calcined for 7 h at 650 °C in an air flux.

2.3. Material Characterization. *2.3.1. Field Emission Scanning Electron Microscopy (FE-SEM).* Surface morphology was evaluated using a field emission scanning electron microscope (ZEISS FE-SEM ULTRA PLUS). For acquisition of all the SEM images, a secondary electron detector (In lens) was used. The accelerating voltage (EHT) applied was 3.00 kV with a resolution (WD) of 2.1 nm. Local compensation of charge (by injecting nitrogen gas) was applied avoiding the sample shading.

2.3.2. High Resolution Transmission Electron Microscopy (H-TEM). Transmission electron microscopy (TEM) was performed using a Philips CM-12 transmission electron microscope equipped with a digital camera MEGA VIEW-II DOCU and operated at 120 kV with magnification of 730 000×. To examine the mesostructure of particles, the samples were embedded in Spurr's resin and cured at 60 °C overnight. The microtomed sections (approximately 100 nm thickness) were cut from the embedded specimen using a diamond knife at room temperature with a RMC PowerTome XL microtome. H-TEM microphotographs were taken using a ZEISS Libra 200 FE OMEGA transmission electron microscope operated at 200 kV with magnification of 1 000 000×. Observations were made in a bright field. Powdered samples were placed on carbon supports of 2000 mesh. The equipment is provided with an electron diffraction (ED) system.

2.3.3. Nitrogen Adsorption Isotherms. The nitrogen adsorption isotherms at −195.4 °C (77.6 K) were measured with a Micrometrics accelerated surface area and porosimetry system (ASAP) model 2020 instrument. Each sample was degassed at 100 °C for 720 min at a pressure of 10^{-4} Pa. To determine the Brunauer−Emmet−Teller (BET) surface area, S_{BET}, the nitrogen molecule diameter is taken as 4.3 Å, calculated by assuming the closest packing spheres,[35] and the area per molecule a_m = 16.2 Å^2.[36] The pore diameter and the pore size distribution were calculated from the adsorption branch of the isotherm by applying the BJH method.[36]

2.3.4. SAXD. The measurements were carried out in a PANalytical-Empyrean type diffractometer, equipped with five-axis goniometer ("χ-φ-*xyz* stage"). X-rays were obtained from a Cu sealed tube type "Empyrean LFFHR Cu". The X-ray radiation was monochromatized with parallel mirror optics type ("crystal, W/Si; graded shape, parabolic acceptance; angle (deg), 0.800; length (mm), 55.3"). The detection of X-rays from the sample is performed using a detector of type area PANalytical Pixcel-3D. XRD measurements were obtained by sweeping the Bragg angles from 0.5 to 5 with a pitch of 0.005 and a time per step of 5 s. The samples were deposited on a support of "zero background" [zero diffraction plate for XRD sample: Si(510)] to ensure that the amorphous component exclusively corresponds to the sample.

DOI: 10.1021/acsami.5b01637
ACS Appl. Mater. Interfaces XXXX, XXX, XXX−XXX

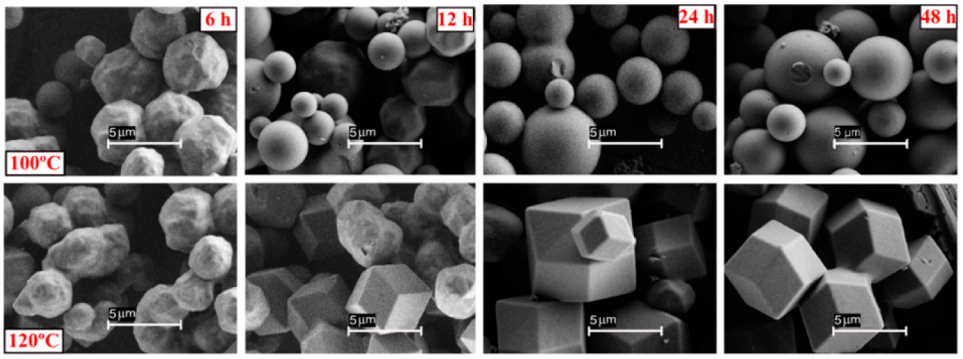

Figure 1. Scanning electron microphotographs of rombdodecahedral and spherical particles synthesized at different time and temperature of hydrothermal treatment. Scale bar = 5 μm.

2.3.5. UV–Vis and Fluorescence Spectroscopy. The UV–vis and fluorescence absorption spectra were recorded at 25 °C by a JASCO V-630 bio spectrophotometer provided with a temperature controller (ETCS-761 JASCO) and by a Varian Cary Eclipse spectrofluorometer, respectively, using a 1 cm path length quartz cell. Both spectra were recorded after the particles' sonication in ethanol to yield homogeneous dispersions. A pure ethanol solution was used as blank.

2.3.6. FT-IR Spectroscopy. FT-IR experiments were done in a Nicolet FT-IR Nexus 470 spectrophotometer. For the avoidance of coadsorbed water, the samples were dried under vacuum until constant weight was achieved and diluted with KBr powder before the FT-IR spectra were recorded.

2.3.7. Computational Modeling. Ab initio calculations based on the density functional theory (DFT)[37] have been performed on crystalline SiO_2 (space group no. 152, $P3_121$, a = 4.9135 Å, c = 5.4050 Å).[38] With that unit cell data, we have fully relaxed the structure using the Wu-Cohen version of the generalized gradient approximation that provides very good bond-length estimates for sp semiconductors.[37] The internal coordinates relax to an average Si–O bond length of 1.62 Å in tetrahedral coordination, with a Si–O–Si bond angle of 141°. This value is in reasonable agreement with those typically reported for other noncrystalline forms of SiO_2.[38] Calculations of the optical conductivity and band gaps used the modified Becke–Johnson exchange-correlation potential,[39] as implemented in the WIEN2k code. This uses a full-potential, all-electron scheme that makes no shape approximation to the electron density or the potential, which is calculated self-consistently without the use of pseudopotentials. The Tran–Blaha modified Becke–Johnson potential was chosen to calculate excited state properties such as band gaps and optical conductivity since it has proven very efficient in determining band gaps of various semiconductors and even the more complicated correlated compounds.[39,40]

3. RESULTS AND DISCUSSION

3.1. SBA-16 Mesoporous Silica Particles. *3.1.1. Particle Characterization.* For the investigation of the morphological and the structural evolution of crystal-like rhombdodecahedral particles, the products originating from the same initial surfactant template mixture were monitored as a function of time and temperature of hydrothermal treatment by SEM, TEM, SAXD, and N_2 adsorption–desorption isotherms.

SEM and TEM images, Figures 1 and 2, reveal that the samples prepared after 24 h of hydrothermal treatment at 100 and 120 °C of temperature are composed by spherical and single-crystal particles of 3.74 ± 1.34 μm and 4.13 ± 0.75 μm in diameter, respectively. Additional SEM images as well as particles size distribution histograms are shown in sections S1–S4 of Supporting Information (SI).

Figure 3 shows the SAXD pattern of polyhedral calcined materials: it displays an intense and broad diffraction peak at

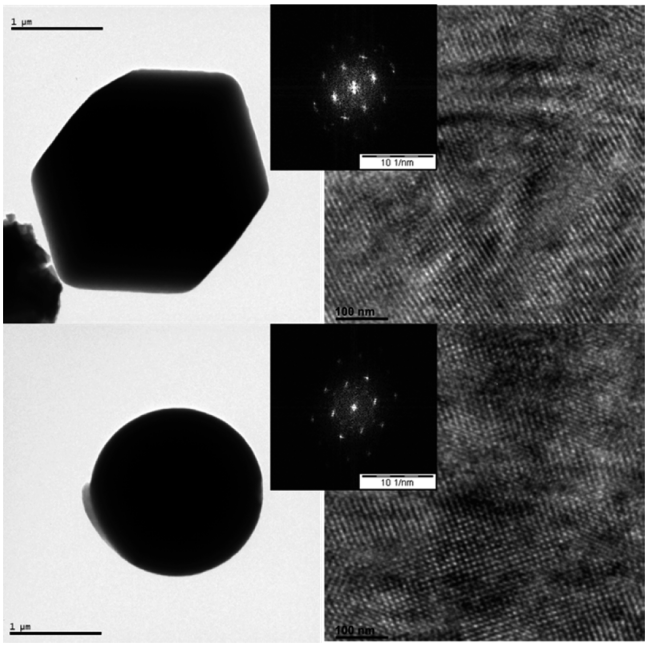

Figure 2. Transmission electron microphotographs of rombdodecahedral and spherical particles. Scale bar: 1 μm. Microtome TEM image of the (110) imaging planes in SBA-16 mesoporous silica crystal (the inset is the Fourier diffractogram). Scale bar: 100 nm.

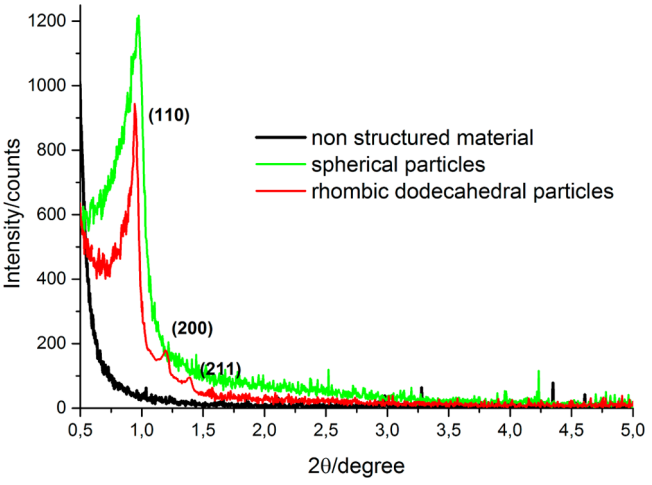

Figure 3. Small angle X-ray diffraction patterns of rombdodecahedral and spherical particles.

DOI: 10.1021/acsami.5b01637
ACS Appl. Mater. Interfaces XXXX, XXX, XXX–XXX

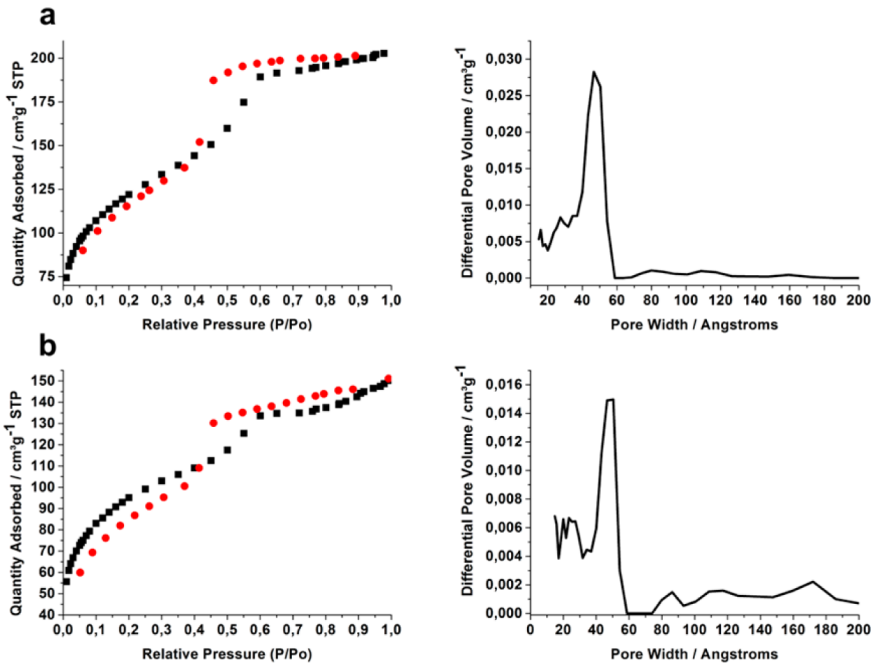

Figure 4. N_2 adsorption−desorption isotherms and pore size distribution computed from the adsorption branch of (a) rombdodecahedral and (b) spherical particles.

about 0.96° followed by two lower intensity signals at 1.25° and 1.40° that are indexed to the (110), (200), and (211) reflections of space group cubic symmetry *Im*3*m*.[13,14] The lower intensity of higher order diffraction peaks are associated with the existence of a high ratio of wall thickness versus pore size and to the roughness of the pore walls.[13] In SBA materials, roughness can be considered quite important due to the large amounts of micropores near to the wall surface and are assigned to be the major cause of lower relative intensities. A high microporosity will result in lower relative intensities. The SAXD spectra of spherical material, Figure 3, show one broad peak assigned to the (110) diffraction, and the absence of higher order signals. The broadening of the first peak and the absence of higher order ones may be explained by a high degree of mesoporosity in the material.[13]

The calcined spherical and polyhedral particles confirmed a type-IV N_2 adsorption−desorption isotherm with a H_2 hysteresis loop (according to IUPAC classification[41]) having an inflection around $P/P_0 \approx 0.4$, Figure 4a,b. Those characteristics describe an ordered mesoporous structure with cylindrical bottle-shaped pore geometry and uniform pore size distributions. Adsorption−desorption hysteresis extends to the lowest attainable pressures; this phenomenon is distinctive of systems containing micropores and may be associated with the swelling of a nonrigid porous structure or with the irreversible uptake of molecules into the pores (or through the pore entrances) of about the same width as that of the adsorbate molecule.[41] A major advance in the interpretation of low hysteresis pressure (LHP) was made by Everett et al.[42] Clear evidence was obtained to associate LHP with some distortion of the adsorbent structure. The proposed theory involves irreversible intercalation of adsorbate molecules in the pores of molecular dimensions leading to inelastic distortion of the adsorbent. In some cases, a slowest relaxation at the operational temperature was appreciated, even when all the intercalating molecules had been removed.[43] A greater difference is seen in the adsorption−desorption branches of the N_2 isotherm for the spherical particles; this fact provides evidence for the lower stability of their ordered mesopore structure in comparison with their polyhedral counterparts.

A narrow pore size distribution (analyzed by using the BJH model[36]) was found for both the adsorption and desorption processes, Figure 4a,b.

Body-centered cubic (bcc) packing of spherical pores seem to be the appropriate model for those materials exhibiting *Im*3*m* symmetry, as the SBA-16.[44] Taking into account such information, two geometrical approximations were applied to obtain independent estimations of the pore size and the wall thickness: the model of spherical cavities and the space-filling polyhedral theory. In the model of spherical cavities, the spherical holes are arranged in a regular collection connected to each other via windows or openings, which are much narrower than the size of the main cavity.[44] The volume fraction of regular cavities is defined as mesoporosity ϵ_{me}:

$$\epsilon_{me} = \frac{\rho_v V_{me}}{1 + \rho_v V_{tot}} \quad (1)$$

Here, ρ_v is the true density of solid walls ($\cong$2.2 g/cm^3 for amorphous siliceous materials), V_{me} is the specific volume of the cavities, and V_{tot} is the total pore volume. The volume of intrawall pores is thus $V_{iw} = V_{tot} - V_{me}$. For a cubic unit cell of length a consisting of ν cavities of diameter D_{me}, the average wall thickness, h, for cubic structures can be calculated from the mesoporosity as

$$D_{me} = a\left(\frac{6}{\pi}\frac{\epsilon_{me}}{\nu}\right)^{1/3} \quad (2)$$

$$h = \frac{D_{me}}{3}\frac{(1 - \epsilon_{me})}{\epsilon_{me}} \quad (3)$$

It follows that, for a 50% mesoporosity, the average wall thickness is equal to two-thirds of the pore radius. ϵ_{me} can be eliminated by substituting $\epsilon_{me} = (\pi/6)D_{me}^3\nu/a^3$:

DOI: 10.1021/acsami.5b01637
ACS Appl. Mater. Interfaces XXXX, XXX, XXX−XXX

$$h = \frac{2a^3}{\pi D_{me}^2 \nu} - \frac{D_{me}}{3} \quad (4)$$

Equation 4 has the advantage of being independent of absolute quantities (per unit weight), and if requires only the knowledge of the characteristic pore size that can be estimated from the capillary condensation pressure. Unlike the spherical cavities model, the space-filling polyhedral theory assumes that the pore shape is polyhedral rather than spherical and that the surface-to-volume ratio can be obtained by the following formula

$$\frac{S_{me}}{V_{me}} = \frac{1}{a}\left(\frac{36\pi\nu}{\xi\epsilon_{me}}\right)^{1/3} \quad (5)$$

where ξ is the isoperimetric quotient defined as

$$\xi = 36\pi V^2/S^3 \quad (6)$$

The values of ξ calculated for *Im*3*m* structure is 0.76.[44] The average wall thickness for the space-filling polyhedral approximation is given by

$$h = 2a\frac{(1-\epsilon_{me})}{\epsilon_{me}}\left(\frac{\xi\epsilon_{me}}{36\pi\nu}\right) \quad (7)$$

For spheres, ξ = 1, and the value of h reduces to that obtained by the application of the spherical model. The structural characteristic parameters of spherical and crystalline SBA-16 mesoporous silica particles as well as the results obtained from application of geometrical models are summarized in Table 1. The hydrothermal treatment affects not only the material's morphology but also the pore size, the wall thickness, the unit cell parameter, and the microporosity. As seen from SAXD measurements, the polyhedral particles prepared at high hydrothermal treatment temperature showed a superior order mesoporosity as compared to that of their spherical analogues. This translates into an increased total surface area, t-plot external surface area, pore surface area, and surface microporosity. Crystalline particles also presented a 77% increase of pore diameter and a 22% decrease in the wall thickness with respect to the spherical ones. As it was noticed in the first article about SBA-15 material,[10] an increase in the hydrothermal time or temperature slightly increases the pore diameter and reduces the silica wall. If we compare the relationship between both materials, the V_μ/V_{tot} ratio, it can be seen that for the rombdodecahedral particles the micropore volume represents only 10% of the total pore volume, while for the spherical particles it exceeds 15%. The S_μ/S_{BET} ratios ≈0.23−0.24 are similar in both obtained materials. The similarity in the V_μ/V_{tot} ratio and S_μ/S_{BET} ratio values indicated that micropores are due to trapped EO chains in the silica walls and are not produced by impressions during the hydrothermal treatment. The two applied geometric models produced similar values, but the space-filling polyhedral theory provided S_{me}/V_{me} values of greater proximity than those obtained from experimental N_2 adsorption−desorption isotherm analysis. On the basis of the obtained results it is supposed that space-filling polyhedral theory, with a certain error, is the best model to describe our materials. Regardless of the model applied, the computed h values are closer to the experimental data obtained for spherical particles.

3.1.2. Basis of the Particle Training Mechanism. Different 1-D silica mesostructures with specific morphologies, including nanorods, nonchiral nanofibers, helical structures,[8] and polyhedral particles,[14,34] were simply achieved by using the triblock copolymer Pluronic F127 and the cationic surfactant CTAB as binary templates. Diverse mechanisms were proposed to explain the silica particle growth, its final morphology, and its mesoporosity by the interaction among hydrolyzed silica species, the surfactant template, and the hydrothermal treatment.[7,8,12,14,34]

The first methodology to generate crystal-like polyhedral SBA-16 mesoporous silica particles using F127 and CTAB as cosurfactant under quiescent conditions was proposed by Mesa and co-workers.[14] The synthesis parameters have been systematically investigated by Poyraz et al.[34] Both authors emphasized the importance of the F127/TEOS, CTAB/F127 molar ratios and the acid conditions on the final morphology.[14,34] In view of the degradation of the copolymer F127 and of the crystalline SBA-16 particles with the increase of the reaction time in acidic conditions presented by Mesa et al.,[14] we have reduced the F127/TEOS = 0.0005 and HCl/TEOS = 1 molar ratios. In addition, we have limited the reaction time to 24 h by the application of a hydrothermal treatment. The CTAB/TEOS = 0.03 molar ratio was conserved as the original synthesis; thus, molar ratios of CTAB/F127 ≈ 62 and H_2O/TEOS ≈ 73 were obtained. These values are superior to those presented by the methodologies of Mesa et al.[14] and Poyraz et al.[34] but consistent with the previously proposed synthesis of

Table 1. Structural Characteristics and Geometrical Model Parameters of SBA-16 Particles

SBA-16 Particle Morphology	spheres	polyhedral
Geometrical Model Parameters		
symmetry group	*Im*3*m*	*Im*3*m*
unit cell, model of packing spherical pores	bcc	bcc
no. cavities per unit cell, ν	2	2
SAXD		
cubic unit cell param[b] a_0/Å, $a_0 = d_{110}\sqrt{2}$	130.00	132.80
wall thickness[b] h/Å, $h = \sqrt[3]{3}\,a_0/2 - d$	85.30	66.50
N_2 Adsorption−Desorption Isotherms		
BET surface area, $S_{BET}/m^2\ g^{-1}$	340.52	435.09
BJH adsorption−desorption cumulative surface area of pores, $S_{pore}/m^2\ g^{-1}$	216.55	346.55
t-plot micropore area, $S_\mu/m^2\ g^{-1}$	77.89	107.32
mesopore area, $S_{me} = S_{pore} - S_\mu/m^2\ g^{-1}$	138.66	239.23
external surface area, $S_{ext} = S_{BET} - S_{pore}/m^2\ g^{-1}$	123.97	88.54
BJH adsorption−desorption cumulative pore volume, $V_{tot}/cm^3\ g^{-1}$	0.18	0.49
t-plot micropore volume, $V_\mu/cm^3\ g^{-1}$	0.03	0.04
mesopore volume, $V_{me} = V_{tot} - V_\mu/cm^3\ g^{-1}$	0.15	0.44
BJH average pore width, d/Å	27.30	48.45
mesopore surface-to-volume ratio, S_{me}/V_{me}/Å $^{-1}$	0.09	0.05
Spherical Cavities Model		
max mesoporosity (close packed limit),[a] $\epsilon_{me}^{max} = \pi\sqrt[3]{3}/8$	0.68	0.68
mesoporosity, ϵ_{me}	0.23	0.47
diameter of regular cavities, D_{me}/Å	78.70	101.70
av wall thickness, h/Å	86.70	38.18
Space-Filling Polyhedral Model		
isoperimetric quotient,[a] ξ	0.76	0.76
mesopore surface-to-volume ratio, S_{me}/V_{me}/Å $^{-1}$	0.08	0.07
av wall thickness, h/Å	78.80	34.80

[a]Data from ref 44. [b]Computed according to ref 14.

DOI: 10.1021/acsami.5b01637
ACS Appl. Mater. Interfaces XXXX, XXX, XXX−XXX

SBA-16 particles.[12,30] According to our suggested synthetic procedure, the CTAB concentration is superior to that of F127 (62 CTAB molecules per molecule of F127). In such conditions, it is a common feature that cationic surfactants interact with Pluronics to form positively charged complex micelles in an aqueous media.[34,45,46] The CTA^+ ions increase the hydrophilicity of the PO−EO interface by incorporating the alkyl tail of the cationic surfactant molecule into the poly(propylene oxide) core and carrying the negatively charged counterions to the PO−EO region. To form mixed micelles in an aqueous media using F127, high CTAB concentrations are needed[34] that are consistent with our proposed methodology. If the process were carried out below the aqueous isoelectric point of silica (IP = 1.7−3.5),[47] cationic silica species ($I^+ = [SiOH_2]^+$) will be present as precursors. Therefore, the key interactions are among the cationic surfactant (S^+), chloride anion (X^-), and cationic silica species ($^+H_2O{-}Si(O-)_3$). From the X-ray diffraction pattern in $2\theta = 0.5-2.5°$ small-angle range (SAXD) measurements, the unit cell parameter and the cubic space group of the particle array of mesopores were determined (Table 1). The obtained values are comparable to those observed in SBA-16 materials templated exclusively by F127 block copolymer in acid media,[34,48] denoting the importance of F127 molecule in the synthesis mechanism. Solubilization of nonionic poly(alkylene oxide) and block copolymer surfactants (S^0) in aqueous media is due to the association of water molecules with the alkylene oxide moieties through hydrogen bonding. This should be enhanced in acid (H^+X^-) media where hydronium ions, instead of water, are associated with the alkylene oxygen atoms, thus adding long-range Coulombic interactions to the coassembly process.[11,14] The assembly might be expected to proceed through an intermediate of the form $(S^0H^+)(X^-I^+)$.[11] The anion may be coordinated directly to the silicon atom through expansion of the silicon atom's coordination sphere. The increment of the sample order with the increase of the hydrothermal treatment temperature can be explained by taking into account the hydrolysis rate of TEOS. Both hydrolysis and condensation reactions are not completed after gel formation when the hydrothermal treatment is started; therefore, reactive silanols are still in the systems, and higher temperature conditions are necessary to accelerate the development of covalent Si−O−Si bonds around the organic species to form ordered structures. During the hydrothermal treatment the hydrophobicity of the EO chains augments with increasing temperature. That is the reason for the changes in pore diameter and wall thickness. The expansion of the hydrophobic core is realized by pushing out the organic layer in the silica walls,[49] so that the hydrophobic chains goe into the hydrophilic core of the micelles and thereby expand them. Expansion of hydrophobic interior and chain retraction from the silica wall result in a reduced microporosity and surface area.[50] The polyhedral particles have surface and total micropore volume values superior than those of the spherical ones. These facts do not contradict the above information; the greater number of micropores is due to the silica condensation, accelerated by temperature, which is the same reason that causes an increase in the mesoporosity order. During the hydrothermal treatment, the EO chains expand the micellar core but do not leave many impressions in the silica walls in comparison with the synthesis at lower initial reaction temperature.[51] Thus, a material with smoother pore walls and a reduced microporosity was obtained; there are though still micropores bridging between the mesopores.

3.2. Hydrothermal Morphogenesis Evolution. Figure 1 shows the time and temperature evolution of silica particles under hydrothermal treatment. At any inspected time and temperature, the observed materials appeared like separate particles: no monolithic forms are obtained. It can be seen that, independent of the applied temperature and before the first 12 h of hydrothermal treatment, the particles possess undefined structures appearing as spherical morphologies. After 24 h of treatment, the morphology advanced to provide spheres or to polyhedral particles depending on the applied temperature. At 120 °C, the particles are uniform in morphology consisting of 12 well-defined rhombic crystal faces indexed to {110} planes forming a rhombdodecahedral figure.[48] No considerable differences in the material morphology were seen after 24 h of hydrothermal treatment. To explain the formation of polyhedral morphologies, the colloidal phase separation mechanism (CPSM) and the multiply twinned particle model (MTP) developed by Ino et al.[52] were used. According to these models, the free energy of the mesophase formation (ΔG) is responsible for the final mesostructure; however, there is a competition between ΔG and the surface free energy of the liquid-crystal-like phase (γ) to determine the particles' final morphology. A single-crystal seed should take an octahedral or tetrahedral shape in order to maximize the expression of {111} facets and minimize γ.[53] As a result, it is not unexpected for a single-crystal seed to evolve into a truncated octahedron (or the so-called Wulff polyhedron) enclosed by eight {111} and six {100} faces.[53] The obtained rhombdodecahedral single-crystal mesoporous particles are composed of 12 {110} facets and represent a high surface energy structure.[53] So, for its formation, it is required to further increase ΔG to overcome the effect of γ. The driving force for the particles' shape evolution seems to be the silica condensation during hydrothermal treatment and the effect of temperature on the hydrophobicity of the PO block chains. As was discussed in the preceding sections, the presence of F127 molecules has a great influence on the mesoporosity and also a great effect on the particle morphology. Abkarian and co-workers[54] analyzed the evolution of spherical to polyhedral shape bubbles that are stable to dissolution in air-saturated water. When particles of volume V_p are modeled as fluid droplets embedded on a larger fluid droplet (the bubble) of volume V, the authors concluded that spherical shape bubbles evolve toward a polyhedral shape with facets as the reduced volume V/V_p is decreased to a certain value. We suppose that the same model can be applied to our system, if we think of a spherical mixed CTAB-copolymer F127 micelle of volume V like a hydrophobic interior of volume V_p and a hydrophilic corona of volume $V_c = V - V_p$, Scheme 1. The hydrophobic interior is composed mainly of the CTA^+ hydrocarbon chains and the PO units, while the hydrated

Scheme 1. Schematic Representation of Temperature Effect on the CTAB-F127 Mixed Micelle Volume

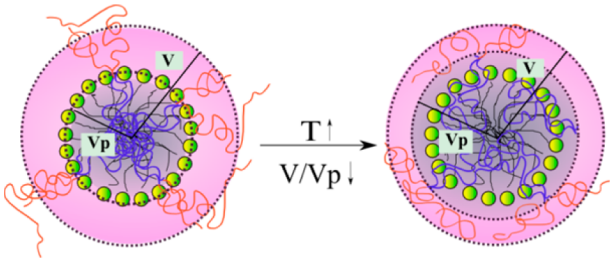

DOI: 10.1021/acsami.5b01637
ACS Appl. Mater. Interfaces XXXX, XXX, XXX−XXX

corona is formed by the EO moieties and the $-N^{+}(CH_3)_3$ polar groups. The lyotropic anions Cl^{-} occupy the hydrophilic regions of Pluronic complex micelles and improved the contribution of PO block enhancing hydrophobic interactions.[34] High temperatures increased hydrophobicity due to the destruction of the hydrogen bond between F127 and water, generating an increment in the hydrophobic core volume, V_p, at the expense of the total volume, V. So, the V/V_p ratio and the V_c diminished. At 120 °C the decrease in the V/V_p ratio and V_c are evidenced in the expansion of mesopore diameter and wall thickness diminution, Table 1, and is high enough to alter the particle morphology. In the model proposed by Abkarian et al.,[54] the configuration of the gas−liquid interface is intimately related to the stability and transformation of the polyhedral bubble. According to the authors the deformation of the interface is a consequence of Newton's law. The presence of repulsive interactions produces an outward normal force on each molecule, because of their confinement on a closed surface. This outward force must be balanced by an inward saddle-shaped deformation of the fluid−fluid interface. This reactive deformation of the interface, which is required for mechanical equilibrium at each volume reduction, leads to a reduction in the Laplace pressure. They emphasize that this saddle-shaped deformation should appear on any initially spherical fluid−fluid interface carrying repulsive particles, as soon as the particles are close enough to interact. We think that an analogy can be applied to the hydrophobic−hydrophilic interface in the CTAB-F127 micelle during the silica hydrolysis and condensation. The interfacial transformation is intimately linked to the processes of hydrolysis and condensation of silica. After 24 h of hydrothermal treatment at 120 °C, the dehydration of EO units and the consequent reduction in micellar volume generate the force that opposes silica's condensation leading to the transformation from spheres to polyhedral particles, Scheme 1.

3.3. Optoelectronic Properties. The band gap energy (E_g) of the rombdodecahedral particles was estimated by plotting $(\alpha h\nu)^m$ against the photon energy ($h\nu$), as shown in Figure 5. No significant adsorption and photoluminescence emissions can be registered for spherical material; see section S5 of Supporting Information. The shape of the particles is associated with a higher order mesoporosity, and according to literature evidence, it is the key point for the superior photoluminescence emission intensity expressed by rombdodecahedral particles.[55] The absorption coefficient, α, is computed by the following relationship[56]

$$\alpha = (2.303 \times 10^3/lc)A\rho_v \quad (8)$$

where A is the measured sample absorption, ρ_v is the amorphous silica density (ρ_v = 2.20 g cm^{-3}[44]), and c is the sample concentration (c = 0.001 75 g cm^{-3}). We assume that the transition of electrons through the forbidden zone occurs between states corresponding to the maximum of the gap and the valence band minimum conductance, taking into account only direct transitions (m = 2). In such conditions, two E_g values (4.95 and 5.70 eV) were determined by extrapolating the adsorption coefficient (α) to zero, Figure 5. The computed values are highly inferior to the band gap associated with an ideal silica lattice (≈ 9 eV),[57] where only Si−O bonds (all Si sites being four-coordinated and all O sites being two-coordinated) are present. It is known that the presence of structural defects in the silica matrix will introduce electronic states into the band gap causing a reduction of E_g. Specifically, there exist three intrinsic defects that are known to introduce electronic states into the band gap: peroxy radicals (POR), nonbridging oxygen hole centers (NBOHC), and E′ centers.[57]

Each of these defect sites has characteristic absorption and photoluminescent (PL) emissions that allow us their identification, Figure 6a,b. Both absorption and emission spectra were deconvoluted into a sum of Gaussian shapes. The absorption spectrum, Figure 6a, is dominated by two high intensity bands centered at 6.1 and 5.6 eV, and a third of middle intensity at 5.4 eV that can be assigned to the presence of E′-centers. The E′-center is defined as an unpaired electron in a dangling tetrahedral (sp^3) orbital of a single silicon atom that is bonded to just three oxygen atoms in the glass network, $\equiv Si^{\bullet}$.[33] It is associated with the 5.85 eV absorption band in

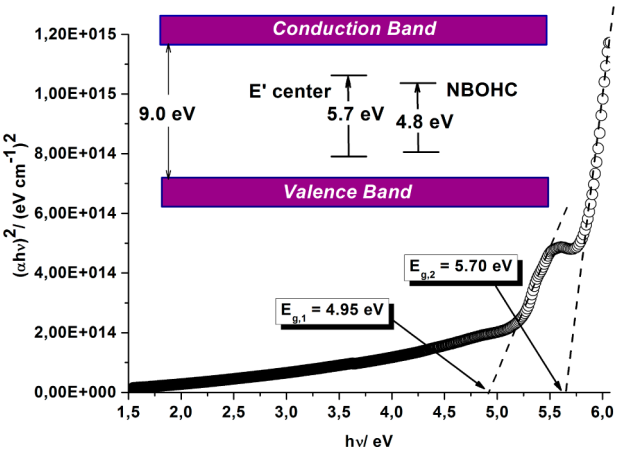

Figure 5. Estimation of band gap energy by plotting $(\alpha h\nu)^2$ vs $h\nu$.

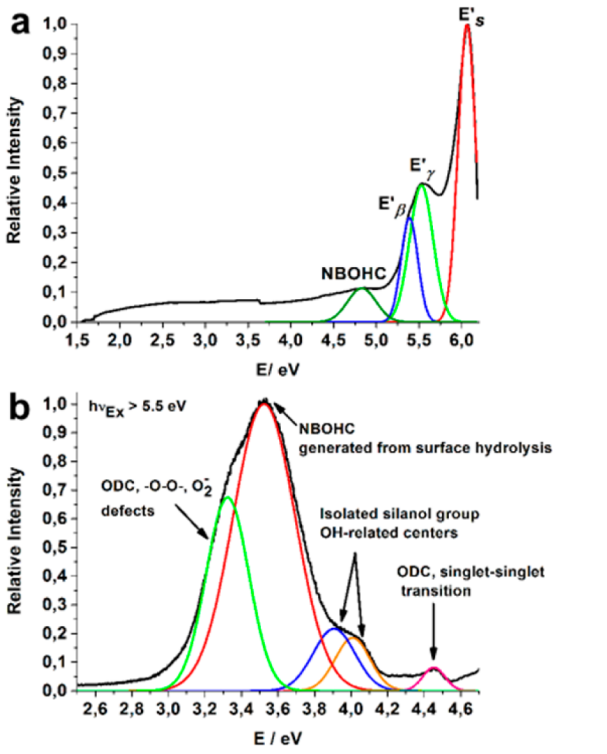

Figure 6. Photoluminescent (a) absorption and (b) emissions of rombdodecahedral particles at room temperature.

DOI: 10.1021/acsami.5b01637
ACS Appl. Mater. Interfaces XXXX, XXX, XXX−XXX

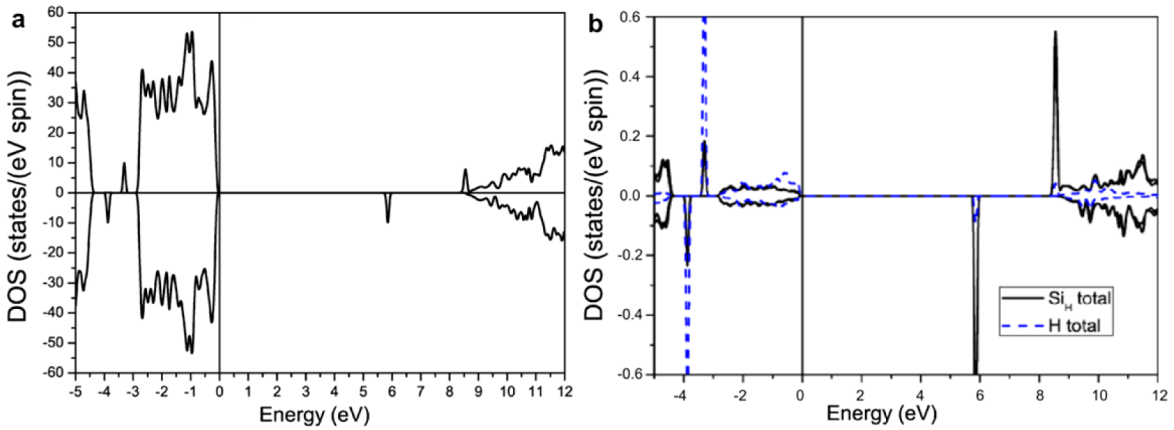

Figure 7. (a) Crystalline SiO_2 density states with one oxygen missing of 24 total oxygens in the unit cell; substituted by a hydrogen atom. Observe the H 1s states at about −3/−4 eV below the Fermi level. (b) Si and H partial density of states. The state in the middle of the gap is an unpaired spin with large SiH character (those two Si atoms neighboring the H dopant).

quartz and silica glass, and no matching emission band has been observed.[33] Four main types of E′-centers, labeled E'_α, E'_β, E'_γ, and E'_s, have been identified in vitreous silica depending on their spectroscopic signatures.[33] The lower intensity peak centered at 5.4 eV was assigned to a E'_β-center,[33] which corresponds to a proton trapped in the oxygen vacancy and the silicon atom containing the unpaired spin relaxed outward. The absorption peak at 5.7 eV resembles an E'_γ-center that consists of a positively charged single oxygen vacancy composed of a nearly planar $\equiv Si^+$ unit and a singly occupied dangling bond $\equiv Si^\bullet$.

An unrelaxed oxygen monovacancy ($\equiv Si\cdots Si\equiv$) or an unperturbed SiO_2 fragment ($\equiv Si—O—Si\equiv$) is assumed to be the precursor of this defect.[33] Finally, the highest intensity peak of the absorption spectra (6.1 eV) matches with a surface E′-center absorption. There exist several variants of surface E′-centers: $E'_s(1)$ which seems like the normal E′-center but with a constant isotropic hyperfine splitting, and a second $E'_s(2)$ which has a dangling silicon bond with a neighboring hydroxyl (OH) group. To further confirm our experimental results and analysis, we have performed DFT-based ab initio calculations in crystalline SiO_2. We have not tried to model all the possible structural defects, but only E'_β as a test of the plausibility of our analysis, see Figures 7 and 8. For pure SiO_2, we have obtained a band gap of about 8.6 eV, in reasonable agreement with experiments (the method used, based on the modified-Becke–Johnson exchange-correlation potential, is particularly suited for yielding accurate band gaps[58]). Introducing a hydrogen atom in place of an oxygen (E'_β-center) and fully relaxing the structure leads to an unpaired electron sitting on a band of Si_H character (those two Si atoms neighboring the H dopant with a Si–H bond distance of about 1.66 Å).

Such a state lies in the middle of the gap with an excitation energy of about 5.8 eV, according to our calculations, in good agreement with experimental evidence. H substituting a missing oxygen is in a H^- $1s^2$ state, as can be seen in the inset of Figure 7, where two H density of states peaks at about 3–4 eV below the Fermi level can be noticed. In our optical conductivity calculations (see Figure 8), above 5.8 eV some additional structure can be seen in the case of H-doping as opposed to the case of pure SiO_2 without defects, Scheme 2. The PL spectra recorded at room temperature for rombdodecahedral particles excited at $h\nu$ = 5.5 eV, Figure 6b, is dominated by a 3.5 eV emission similar to the observed ultraviolet emissions of

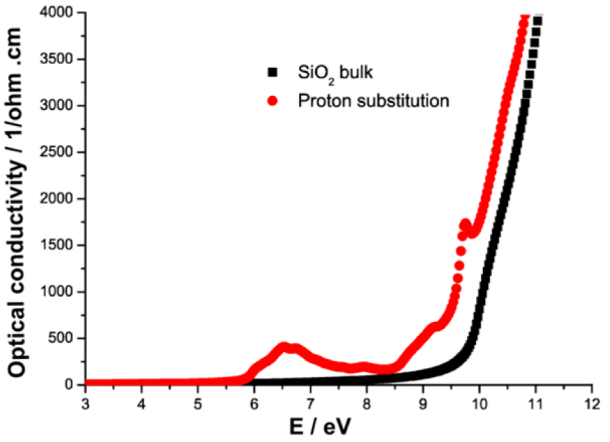

Figure 8. Optical conductivity of pure crystalline SiO_2 and a supercell of SiO_2 with one oxygen missing out of 24 total oxygens in the supercell, substituted by a hydrogen atom. Observe the structure in the doped case appearing above 5.8 eV, the excitation energy of the hydrogen defect.

Scheme 2. Representation of the SiO_2 Structure Highlighting the Hydrogen Atom in the Place of Oxygen

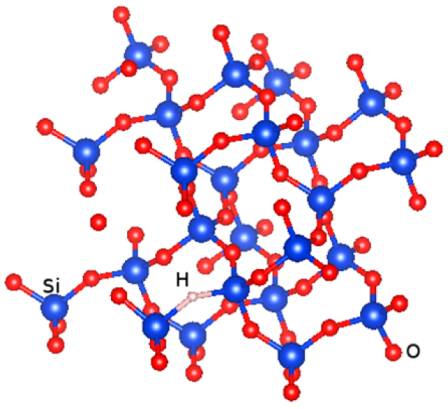

oxidized porous silicon (OPS) and silicon nanostructures (SNS).[59] The E′ centers, previously identified in the absorption spectra, are characterized by a well-assessed experimental lack of any PL emission in bulk silica.[33,60] Although some theoretical calculations suggest that surface variants of the E′-center might

DOI: 10.1021/acsami.5b01637
ACS Appl. Mater. Interfaces XXXX, XXX, XXX–XXX

decay through radiative transitions, the assignment of the 3.5 eV PL emission to surface E′-like structures cannot be made on the basis of such information. Different attributions like small silicon clusters consisting of Si sites surrounded by four adjacent silicon atoms sharing one or two electrons,[61] oxygen deficient centers (ODC) at the interface of Si nanoclusters,[59,62] or the presence of apical-like surfaces centers distinct to E′-centers have been proposed[60] to explain the 3.5 eV PL emission. In all cases PL emissions are dependent on the material specific surface and related to surface emitting centers. Because the rombdodecahedral particles are characterized by a large value of the surface/volume ratio, we assume that these kinds of centers are responsible for the UV-PL.

Yao et al.[63] observed an UV-PL emission at around 330 nm (3.6 eV) in porous silica prepared by the sol−gel method that is associated with the presence of surface −OH groups. To correlate the UV-PL with hydroxyls, we analyze the infrared absorption spectra of rombdodecahedral particles, Figure 9.

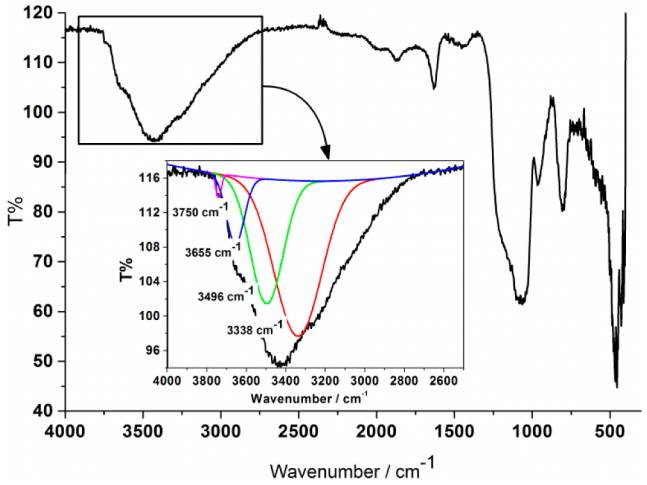

Figure 9. FT-IR spectra of rombdodecahedral particles. Inset: Deconvolution of the broad band from 4800 to 3000 cm^{-1}.

The FTIR spectra exhibit strong absorption bands associated with the characteristic stretching, bending, and wagging vibrations of SiO_2 groups at 1090, 806, and 467 cm^{-1}, respectively.[63]

The broad band from 4800 to 3000 cm^{-1} is attributed to the −OH stretching vibration. This zone was deconvoluted into several Gaussian bands assigned to the existence of different −OH groups in the silica matrix. The band at 3750 cm^{-1} is attributed to the vibration of surface isolated silanol groups,[63] while the bands at 3655 and 3496 cm^{-1} correspond to different vicinal OH-groups.[64] The wide band that peaked at 3338 cm^{-1} is coming from the silanol groups on the surface which are hydrogen bonded to atmospheric molecular water. Accordingly, the band present at 1636 cm^{-1} is due to the bending vibration of the water molecule. The presence of −OH groups also can be supported by the presence of two PL-emissions that peaked at 4.01 and 4.4 eV and correspond to isolated silanol and OH-related centers, Figure 6b. Hydroxyls are believed to be a precursor for NBOHC, which can be created by the heat treatment of silica in air at T_{ht} > 600 °C.[63] The NBOHC has a characteristic adsorption band at 4.8 eV, which can be identified as a band of low intensity in the absorption spectra, Figure 6a. Moreover, the proximity of the NBOHC absorption band to that with the obtained E_g = 4.95 eV and the fact that it is one of the three intrinsic defects that are known to introduce electronic states into the band gap might suggest that the defect responsible for the 3.5 eV may correlate with NBOHCs generated from surface adjacent and isolated hydroxyls similar to those found by Yao et al.[63] The NBOHC defect can be visualized as the oxygen part of a broken bond. It is electrically neutral and paramagnetic and represents the simplest elementary oxygen related intrinsic defect in silica. The most unique fingerprint of this center is the 1.9 eV photoluminescent band in the red region of the visible light spectra. By inspection of PL emission spectra, it can be seen that 1.9 eV PL band characteristic of the above-mentioned point defect is not present. However, Yao et al.[63] based on the work of Glinka and co-workers[65] determined that NBOHCs (C_1^0) could be charge modified (C_1^+) by exciting one electron from the C_1^0 to the conduction band. Then, C_1^+ is involved in a recombination process leading to an emission at 3.75 eV similar to that we have registered. Other bands of minor intensity are identified in absorption spectra with the correspondent PL emissions that are assigned to different diamagnetic oxygen-deficient centers (ODC).

The shape of emission spectra is sensitive to the photon excitation energy as we can appreciate from the inspection of the PL−PL emission (PLE) pattern of rombdodecahedral particles at room temperature, Figure 10. This is related to the

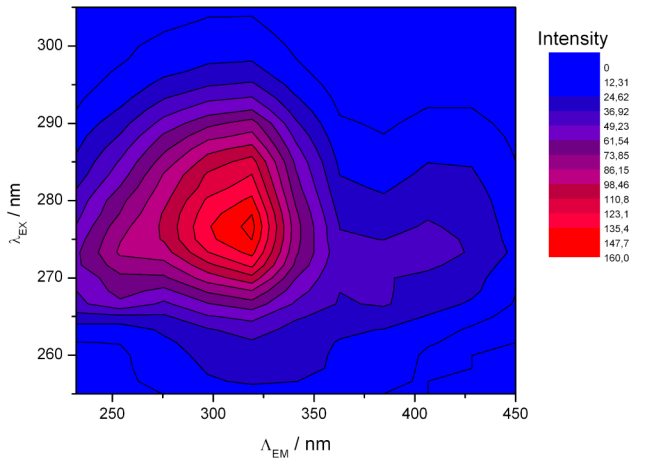

Figure 10. PL−PL excitation patterns of rombdodecahedral particles.

presence of overlapped levels in the material rather than one specific defect with a well-localized energy level, which is in agreement with our previous results.

4. CONCLUSION

Morphology-controlled synthesis of crystal-like rombdodecahedral particles (≈5 μm) showing SBA-16 mesoporosity and ultraviolet photoluminescence emissions at room temperature has been successfully achieved by the use of a low consuming reagent hydrothermal synthetic method. The direction of the mesoporous structure as well as the morphology of the material were achieved through the synergistic effect of the binary mixture of surfactants (CTAB/F127) employed under specific reaction conditions. The hydrophobic variability of the F127 molecule subjected to the hydrothermal treatment conditions has a key role on the formation of both the particle's crystal-like external morphology as well as the cubic mesophase responsible for the ordered arrangement of mesopores.

DOI: 10.1021/acsami.5b01637
ACS Appl. Mater. Interfaces XXXX, XXX, XXX−XXX

Meanwhile the cationic molecule favors the interaction with the silica precursor and exerts a protective effect to the F127 degradation in acidic media. As a consequence of their internal mesoporosity order, rombdodecahedral particles show definite absorptions and photoluminescence emissions in the ultraviolet region at room temperature. Our experimental and theoretical comparative studies allow us to infer that the presence of intrinsic defects confined into an ordered mesoporous structure plays a very important role in semiconductor materials. They are able to change their electronic and optical properties making them functional for a vast amount of applications.

■ ASSOCIATED CONTENT

Supporting Information

Scanning electron microphotographs, size distribution histograms, and UV adsorption bands of spherical and rombdodecahedral particles. The Supporting Information is available free of charge on the ACS Publications website at DOI: 10.1021/acsami.5b01637.

■ AUTHOR INFORMATION

Corresponding Author

*Phone: +54 291 4595159. Fax: +54 291 4595160. E-mail: pmessina@uns.edu.ar.

Notes

The authors declare no competing financial interest.

■ ACKNOWLEDGMENTS

The authors acknowledge Universidad Nacional del Sur (PGI 24/Q064), Concejo Nacional de Investigaciones Científicas y Técnicas de la República Argentina (CONICET, PIP-11220130100100CO), and Fundación Ramón Areces. N.L.D., N.G., and J.S. have doctoral fellowships from CONICET. P.V.M. is an independent researcher from CONICET. V.P. acknowledges support from the Spanish Government through the Ramón y Cajal Program, the Xunta de Galicia through Project EM2013/037 and MINECO (Project No. MAT2013-44673-R).

■ REFERENCES

(1) Agarwal, U.; Escobedo, F. A. Mesophase Behaviour of Polyhedral Particles. *Nat. Mater.* **2011**, *10*, 230−235.

(2) Niu, W.; Zheng, S.; Wang, D.; Liu, X.; Li, H.; Han, S.; Chen, J.; Tang, Z.; Xu, G. Selective Synthesis of Single-Crystalline Rhombic Dodecahedral, Octahedral, and Cubic Gold Nanocrystals. *J. Am. Chem. Soc.* **2009**, *131*, 697−703.

(3) Liu, W.; Zhu, Z.; Deng, K.; Li, Z.; Zhou, Y.; Qiu, H.; Gao, Y.; Che, S.; Tang, Z. Gold Nanorod@Chiral Mesoporous Silica Core−Shell Nanoparticles with Unique Optical Properties. *J. Am. Chem. Soc.* **2013**, *135*, 9659−9664.

(4) Deng, Y.; Liu, C.; Liu, J.; Zhang, F.; Yu, T.; Zhang, F.; Gu, D.; Zhao, D. A Novel Approach to the Construction of 3-D Ordered Macrostructures with Polyhedral Particles. *J. Mater. Chem.* **2008**, *18*, 408−415.

(5) Zhu, Z.; Meng, H.; Liu, W.; Liu, X.; Gong, J.; Qiu, X.; Jiang, L.; Wang, D.; Tang, Z. Superstructures and SERS Properties of Gold Nanocrystals with Different Shapes. *Angew. Chem.* **2011**, *123*, 1631−1634.

(6) Kresge, C. T.; Leonowicz, M. E.; Roth, W. J.; Vartuli, J. C.; Beck, J. S. Ordered Mesoporous Molecular Sieves Synthesized by a Liquid-Crystal Template Mechanism. *Nature* **1992**, *359*, 710−712.

(7) Han, L.; Xiong, P.; Bai, J.; Che, S. Spontaneous Formation and Characterization of Silica Mesoporous Crystal Spheres with Reverse Multiply Twinned Polyhedral Hollows. *J. Am. Chem. Soc.* **2011**, *133*, 6106−6109.

(8) Ye, J.; Zhang, H.; Yang, R.; Li, X.; Qi, L. Morphology-Controlled Synthesis of SnO_2 Nanotubes by Using 1D Silica Mesostructures as Sacrificial Templates and Their Applications in Lithium-Ion Batteries. *Small* **2010**, *6*, 296−306.

(9) Vinu, A.; Mori, T.; Ariga, K. New Families of Mesoporous Materials. *Sci. Technol. Adv. Mater.* **2006**, *7*, 753−771.

(10) Zhao, D.; Feng, J.; Huo, Q.; Melosh, N.; Fredrickson, G. H.; Chmelka, B. F.; Stucky, G. D. Triblock Copolymer Syntheses of Mesoporous Silica with Periodic 50 to 300 Angstrom Pores. *Science* **1998**, *279*, 548−552.

(11) Zhao, D.; Huo, Q.; Feng, J.; Chmelka, B.; Stucky, G. Nonionic Triblock and Star Diblock Copolymer and Oligomeric Surfactant Syntheses of Highly Ordered, Hydrothermally Stable, Mesoporous Silica Structures. *J. Am. Chem. Soc.* **1998**, *120*, 6024−6036.

(12) Yu, C.; Fan, J.; Tian, B.; Zhao, D. Morphology Development of Mesoporous Materials: A Colloidal Phase Separation Mechanism. *Chem. Mater.* **2004**, *16*, 889−898.

(13) Stevens, W. J. J.; Lebeau, K.; Mertens, M.; Van Tendeloo, G.; Cool, P.; Vansant, E. F. Investigation of the Morphology of the Mesoporous SBA-16 and SBA-15 Materials. *J. Phys. Chem. B* **2006**, *110*, 9183−9187.

(14) Mesa, M.; Sierra, L.; Patarin, J.; Guth, J.-L. Morphology and Porosity Characteristics Control of SBA-16 Mesoporous Silica. Effect of the Triblock Surfactant Pluronic F127 Degradation During the Synthesis. *Solid State Sci.* **2005**, *7*, 990−997.

(15) Wan, Y.; Zhao. On the Controllable Soft-Templating Approach to Mesoporous Silicates. *Chem. Rev.* **2007**, *107*, 2821−2860.

(16) Velev, O. D.; Lenhoff, A. M.; Kaler, E. W. A Class of Microstructured Particles Through Colloidal Crystallization. *Science* **2000**, *287*, 2240−2243.

(17) Li, F.; Badel, X.; Linnros, J.; Wiley, J. B. Fabrication of Colloidal Crystals with Tubular-like Packings. *J. Am. Chem. Soc.* **2005**, *127*, 3268−3269.

(18) Lin, Y. S.; Hung, Y.; Lin, H. Y.; Tseng, Y. H.; Chen, Y. F.; Mou, C. Y. Photonic Crystals from Monodisperse Lanthanide-Hydroxide-at-Silica Core/Shell Colloidal Spheres. *Adv. Mater.* **2007**, *19*, 577−580.

(19) Li, Y.; He, Y.; Tong, X.; Wang, X. Photoinduced Deformation of Amphiphilic Azo Polymer Colloidal Spheres. *J. Am. Chem. Soc.* **2005**, *127*, 2402−2403.

(20) Kim, J.-W.; Larsen, R. J.; Weitz, D. A. Synthesis of Nonspherical Colloidal Particles with Anisotropic Properties. *J. Am. Chem. Soc.* **2006**, *128*, 14374−14377.

(21) Grosso, D.; de A. A. Soler-Illia, G. J.; Babonneau, F.; Sanchez, C.; Albouy, P. A.; Brunet-Bruneau, A.; Balkenende, A. R. Highly Organized Mesoporous Titania Thin Films Showing Mono-Oriented 2D Hexagonal Channels. *Adv. Mater.* **2001**, *13*, 1085−1090.

(22) Kim, J.; Lee, J. E.; Lee, J.; Yu, J. H.; Kim, B. C.; An, K.; Hwang, Y.; Shin, C.-H.; Park, J.-G.; Kim, J.; Hyeon, T. Magnetic Fluorescent Delivery Vehicle Using Uniform Mesoporous Silica Spheres Embedded with Monodisperse Magnetic and Semiconductor Nanocrystals. *J. Am. Chem. Soc.* **2005**, *128*, 688−689.

(23) Su, C.-Y.; Goforth, A. M.; Smith, M. D.; Pellechia, P. J.; zur Loye, H.-C. Exceptionally Stable, Hollow Tubular Metal−Organic Architectures: Synthesis, Characterization, and Solid-State Transformation Study. *J. Am. Chem. Soc.* **2004**, *126*, 3576−3586.

(24) Kleitz, F.; Marlow, F.; Stucky, G. D.; Schüth, F. Mesoporous Silica Fibers: Synthesis, Internal Structure, and Growth Kinetics. *Chem. Mater.* **2001**, *13*, 3587−3595.

(25) Wu, X.; Ruan, J.; Ohsuna, T.; Terasaki, O.; Che, S. A Novel Route for Synthesizing Silica Nanotubes with Chiral Mesoporous Wall Structures. *Chem. Mater.* **2007**, *19*, 1577−1583.

(26) Man Kim, J.; Ryoo, R. Synthesis of MCM-48 Single Crystals. *Chem. Commun.* **1998**, *2*, 259−260.

(27) Guan, S.; Inagaki, S.; Ohsuna, T.; Terasaki, O. Cubic Hybrid Organic−Inorganic Mesoporous Crystal with a Decaoctahedral Shape. *J. Am. Chem. Soc.* **2000**, *122*, 5660−5661.

DOI: 10.1021/acsami.5b01637
ACS Appl. Mater. Interfaces XXXX, XXX, XXX−XXX

(28) Sayari, A.; Hamoudi, S.; Yang, Y.; Moudrakovski, I. L.; Ripmeester, J. R. New Insights into the Synthesis, Morphology, and Growth of Periodic Mesoporous Organosilicas. *Chem. Mater.* **2000**, *12*, 3857−3863.
(29) Che, S.; Sakamoto, Y.; Terasaki, O.; Tatsumi, T. Control of Crystal Morphology of SBA-1 Mesoporous Silica. *Chem. Mater.* **2001**, *13*, 2237−2239.
(30) Yu, C.; Tian, B.; Fan, J.; Stucky, G. D.; Zhao, D. Nonionic Block Copolymer Synthesis of Large-Pore Cubic Mesoporous Single Crystals by Use of Inorganic Salts. *J. Am. Chem. Soc.* **2002**, *124*, 4556−4557.
(31) Hassan, N.; Verdinelli, V.; Ruso, J. M.; Messina, P. V. Mimicking Natural Fibrous Structures of Opals by Means of a Microemulsion-Mediated Hydrothermal Method. *Langmuir* **2011**, *27*, 8905−8912.
(32) Ruso, J. M.; Gravina, A. N.; D'Elia, N. L.; Messina, P. V. Highly Efficient Photoluminescence of SiO_2 and Ce-SiO_2 Microfibres and Microspheres. *Dalton Trans.* **2013**, *42*, 7991−8000.
(33) Salh, R. Defect Related Luminescence in Silicon Dioxide Network: A Review. In *Crystalline Silicon: Properties and Uses*; Basu, S., Ed.; InTech: Rijeka, Croatia, 2011; pp 135−172.
(34) Poyraz, A. S.; Albayrak, C.; Dag, Ö. The Effect of Cationic Surfactant and Some Organic/Inorganic Additives on the Morphology of Mesostructured Silica Templated by Pluronics. *Microporous Mesoporous Mater.* **2008**, *115*, 548−555.
(35) Lippens, B. C.; Linsen, B. G.; Boer, J. H. d. Studies on Pore Systems in Catalysts I. The Adsorption of Nitrogen; Apparatus and Calculation. *J. Catal.* **1964**, *3*, 32−37.
(36) Barrett, E. P.; Joyner, L. G.; Halenda, P. P. The Determination of Pore Volume and Area Distributions in Porous Substances. I. Computations from Nitrogen Isotherms. *J. Am. Chem. Soc.* **1951**, *73*, 373−380.
(37) Hohenberg, P.; Kohn, W. Inhomogeneous Electron Gas. *Phys. Rev.* **1964**, *136*, B864−B871.
(38) Helms, C. R.; Poindexter, E. H. The Silicon-Silicon Dioxide System: Its Microstructure and Imperfections. *Rep. Prog. Phys.* **1994**, *57*, 791.
(39) Tran, F.; Blaha, P. Accurate Band Gaps of Semiconductors and Insulators with a Semilocal Exchange-Correlation Potential. *Phys. Rev. B* **2009**, *102*, 226401.
(40) Botana, A. S.; Tran, F.; Pardo, V.; Baldomir, D.; Blaha, P. Electronic Structure of CrN: A Comparison Between Different Exchange Correlation Potentials. *Phys. Rev. B* **2012**, *85*, 235118.
(41) Sing, K. S. W.; Everett, D. H.; Haul, R. A. W.; Moscou, L.; Pierotti, R. A.; Rouquérol, J.; Semieniewska, T. Recommendations for the Characterization of Porous Solids. *Pure Appl. Chem.* **1985**, *66*, 1739−1758.
(42) Everett, D. H.; Powl, J. C. Adsorption in Slit-like and Cylindrical Micropores in the Henry's Law Region. A Model for the Microporosity of Carbons. *J. Chem. Soc., Faraday Trans. 1* **1976**, *72*, 619−636.
(43) Rouquerol, F; Rouquerol, J.; Sing, K. S. W.; Llewellyn, P.; Maurin, G. *Adsorption by Powders and Porous solids, principles, Methodology and Applications*, 2nd ed.; Academic Press.: Oxford, U.K., 2014; p 646.
(44) Ravikovitch, P. I.; Neimark, A. V. Density Functional Theory of Adsorption in Spherical Cavities and Pore Size Characterization of Templated Nanoporous Silicas with Cubic and Three-Dimensional Hexagonal Structures. *Langmuir* **2002**, *18*, 1550−1560.
(45) Li, Y.; Xu, R.; Couderc, S.; Bloor, D. M.; Holzwarth, J. F.; Wyn-Jones, E. Binding of Tetradecyltrimethylammonium Bromide to the ABA Block Copolymer Pluronic F127 (EO97 PO69 EO97): Electromotive Force, Microcalorimetry, and Light Scattering Studies. *Langmuir* **2001**, *17*, 5742−5747.
(46) Jansson, J.; Schillén, K.; Nilsson, M.; Söderman, O.; Fritz, G.; Bergmann, A.; Glatter, O. Small-Angle X-ray Scattering, Light Scattering, and NMR Study of PEO−PPO−PEO Triblock Copolymer/Cationic Surfactant Complexes in Aqueous Solution. *J. Phys. Chem. B* **2005**, *109*, 7073−7083.
(47) Iker, R. K. *The Chemistry of Silica: Solubility, Polymerization, Colloids and Surface Properties and Biochemistry*; Wiley: New York, 1979.
(48) Lin, C.-L.; Pang, Y.-S.; Chao, M.-C.; Chen, B.-C.; Lin, H.-P.; Tang, C.-Y.; Lin, C.-Y. Synthesis of SBA-16 and SBA-15 Mesoporous Silica Crystals Templated with Neutral Block Copolymer Surfactants. *J. Phys. Chem. Solids* **2008**, *69*, 415−419.
(49) Kruk, M.; Cao, L. Pore Size Tailoring in Large-Pore SBA-15 Silica Synthesized in the Presence of Hexane. *Langmuir* **2007**, *23*, 7247−7254.
(50) Galarneau, A.; Cambon, H.; Di Renzo, F.; Fajula, F. True Microporosity and Surface Area of Mesoporous SBA-15 Silicas as a Function of Synthesis Temperature. *Langmuir* **2001**, *17*, 8328−8335.
(51) Van Der Voort, P.; Ravikovitch, P. I.; De Jong, K. P.; Benjelloun, M.; Van Bavel, E.; Janssen, A. H.; Neimark, A. V.; Weckhuysen, B. M.; Vansant, E. F. A New Templated Ordered Structure with Combined Micro- and Mesopores and Internal Silica Nanocapsules. *J. Phys. Chem. B* **2002**, *106*, 5873−5877.
(52) Ino, S. Stability of Multiply-Twinned Particles. *J. Phys. Soc. Jpn.* **1966**, *27*, 941−953.
(53) Lim, B.; Jiang, M.; Tao, J.; Camargo, P. H. C.; Zhu, Y.; Xia, Y. Shape-Controlled Synthesis of Pd Nanocrystals in Aqueous Solutions. *Adv. Funct. Mater.* **2009**, *19*, 189−200.
(54) Abkarian, M.; Subramaniam, A. B.; Kim, S.-H.; Larsen, R. J.; Yang, S.-M.; Stone, H. A. Dissolution Arrest and Stability of Particle-Covered Bubbles. *Phys. Rev. Lett.* **2007**, *99*, 188301.
(55) Glinka, Y. D.; Lin, S.-H.; Hwang, L.-P.; Chen, Y.-T. Photoluminescence Spectroscopy of Silica-Based Mesoporous Materials. *J. Phys. Chem. B* **2000**, *104*, 8652−8663.
(56) Serpone, N.; Lawless, D.; Khairutdinov, R. Size Effects on the Photophysical Properties of Colloidal Anatase TiO2 Particles: Size Quantization versus Direct Transitions in This Indirect Semiconductor? *J. Phys. Chem.* **1995**, *99*, 16646−16654.
(57) Gimon-Kinsel, M. E.; Groothuis, K.; Balkus, K. J., Jr. Photoluminescent Properties of MCM-41 Molecular Sieves. *Microporous Mesoporous Mater.* **1998**, *20*, 67−76.
(58) Koller, D.; Tran, F.; Blaha, P. Merits and Limits of the Modified Becke-Johnson Exchange Potential. *Phys. Rev. B* **2011**, *83*, 195134.
(59) Qin, G. G.; Lin, J.; Duan, J. Q.; Yao, G. Q. A Comparative Study of Ultraviolet Emission with Peak Wavelengths Around 350 nm from Oxidized Porous Silicon and That from SiO_2 Powder. *Appl. Phys. Lett.* **1996**, *69*, 1689−1691.
(60) Chiodini, N.; Meinardi, F.; Morazzoni, F.; Paleari, A.; Scotti, R.; Di Martino, D. Ultraviolet Photoluminescence of Porous Silica. *Appl. Phys. Lett.* **2000**, *76*, 3209−3211.
(61) Kim, K.; Suh, M. S.; Kim, T. S.; Youn, C. J.; Suh, E. K.; Shin, Y. J.; Lee, K. B.; Lee, H. J.; An, M. H.; Ryu, H. Room-Temperature Visible Photoluminescence from Silicon-Rich Oxide Layers Deposited by an Electron Cyclotron Resonance Plasma Source. *Appl. Phys. Lett.* **1996**, *69*, 3908−3910.
(62) Song, H. Z.; Bao, X. M.; Li, N. S.; Wu, X. L. Strong Ultraviolet Photoluminescence from Silicon Oxide Films Prepared by Magnetron Sputtering. *Appl. Phys. Lett.* **1998**, *72*, 356−358.
(63) Yao, B.; Shi, H.; Zhang, X.; Zhang, L. Ultraviolet Photoluminescence from Nonbridging Oxygen Hole Centers in Porous Silica. *Appl. Phys. Lett.* **2001**, *78*, 174−176.
(64) Zhuravlev, L. T. The Surface Chemistry of Amorphous Silica. Zhuravlev Model. *Colloids Surf., A* **2000**, *173*, 1−38.
(65) Glinka, Y. D.; Degoda, V. Y.; Naumenko, S. N. Multiphoton Mechanism of Generation of Elementary Excitations in Disperse SiO_2. *J. Non-Cryst. Solids* **1993**, *152*, 219−224.

DOI: 10.1021/acsami.5b01637
ACS Appl. Mater. Interfaces XXXX, XXX, XXX−XXX